Materials Transactions, Vol. 49, No. 7 (2008) pp. 1629 to 1637

Microstructure and Mechanical Properties of Resistance Spot Welded Advanced High Strength Steels

M. I. Khan[1], M. L. Kuntz[1], E. Biro[2] and Y. Zhou[1]

[1]*University of Waterloo, Ontario, Canada*
[2]*ArcelorMittal Dofasco Research, Ontario, Canada*

Integration of advanced high strength steels (AHSS) into the automotive architecture has brought renewed challenges for achieving acceptable welds. Resistance spot welding (RSW) is the primary method used in welding automotive structures, which has resulted in a demand to better understand RSW of AHSS. The varying alloy contents and processing techniques used in their production has further complicated this initiative. The current study examines resistance spot welding of AHSS including 590R, DP600, DP780 and TRIP780. HSLA material is also included to represent conventional high strength steels and benchmark AHSS performance. The mechanical properties and microstructure of these resistance welded steel alloys are detailed. Furthermore, a relationship between chemistries and fusion zone hardness is produced.
[doi:10.2320/matertrans.MRA2008031]

(Received January 22, 2008; Accepted April 10, 2008; Published May 28, 2008)

Keywords: *resistance spot welding, microstructure and mechanical properties, dual phase steels, transformation induced plasticity steel, ferritic-bainitic steel, high strength low alloy steel*

1. Introduction

Resistance spot welding (RSW) is the predominant welding technique used for joining steel in automotive applications. New developments in advanced high strength steels (AHSS) have helped reduce weight, improve fuel efficiency, and increase the crashworthiness of vehicles through enhanced mechanical properties. This has accelerated the integration of AHSS into the automotive architecture and increased demands to understand the effects of RSW. As a result, there has been a recent focus on the weldability of these steels.

The various grades of AHSS have unique chemistries and undergo distinct processing techniques compared to conventional high strength steels (HSS). Rich chemistries, inherent to AHSS, aid in producing base metal microstructures which improve the strength and, in some cases, ductility of these alloys. The typical yield strength of high strength low alloy steels (HSLA) is below 500 MPa, which classifies them as HSS. Extensive research on the weldability of HSLA has resulted in its effective integration into the automotive architecture. Hence, effects during welding HSLA steel alloys have been extensively examined.[1–3] Compared to conventional HSS, the weldability of AHSS is not yet fully understood.

There are several types of AHSS which can be classified according to the processing, microstructure, and mechanical properties of the material. The most common types currently in use include dual phase (DP), transformation induced plasticity (TRIP), and ferritic-bainitic (FB) AHSS. Characteristics of the ferritic-bainitic 590R include enhanced formability coupled with high strength. Development of this new steel was based on achieving a stable weldable alloy with relatively low levels of carbon and alloying elements.[4] Studies have shown potential in replacing conventional 440 MPa steel with thinner gauge 590R which exhibits higher energy absorption during impact.[4,5]

DP steels have high strength-to-weight ratios, and are ideal for automotive applications. The typical DP microstructure consists of hard martensite islands surrounded with a soft ferrite matrix. The strength of DP steels is generally proportional to the volume fraction of martensite; increased volume fractions have been shown to increase the strength of DP steels.[6] Furthermore, improved formability and strechability of certain DP grades makes them ideal for replacing thicker conventional HSS.

TRIP steels exhibit high strengths and excellent formability. Typical TRIP microstructure consists of metastable retained austenite and finely dispersed bainite surrounded by a ferrite matrix. Decomposition of the austenite phase into martensite during plastic deformation has been shown to improve ductility. However, the relatively rich chemistries required to produce TRIP steels have increased the complexity of the weld microstucture compared to conventional HSS.

Since the RSW process is the primary joining method used in automotive production, a detailed understanding of metallurgical changes and their effects on the mechanical performance of AHSS welds is required for safe integration into the automotive architecture. Recent publications detailing microstructure and mechanical properties of resistance welded AHSS have usually focused exclusively on describing the response of a single grade of steel. For example, Marya *et al.*[7] examined the effects of RSW process parameters on the failure mode during tensile shear testing of DP steels. Similarly, Tong *et al.*[8] examined the mechanical properties of spot welded DP steels and their influence on failure behavior. The current literature, however, fails to critically compare the microstructure and mechanical properties of spot weldments in various different grades of AHSS.

The objectives of the current study are to detail and compare the microstructure and static mechanical properties of RSW AHSS, and to benchmark them against welds in HSLA. The examined steels include: an HSLA, 590R, DP600, DP780 and TRIP780. The measurement of weld properties in various steels will be used to construct a model to predict fusion zone hardness after RSW. Analysis of the impact performance of these steels is presented in a separate publication.[9]

Table 1 Material Properties.

Steel Grade	Thickness	Coating		Alloying elements %					C.E.
		Type	Ave. Wt.	C	Mn	Mo	Cr	Si	
HSLA	1.00 mm	GI	73.9 g/m^2	0.060	0.640	0.010	0.050	0.240	**0.139**
590 R	1.20 mm	GA	43.4 g/m^2	0.130	1.599	0.013	0.029	0.120	**0.363**
DP600	1.20 mm	GI	55.1 g/m^2	0.100	1.523	0.196	0.197	0.157	**0.326**
DP780	1.15 mm	GA	58.8 g/m^2	0.113	2.082	0.181	0.239	0.036	**0.427**
TRIP780	1.00 mm	GI	62.5 g/m^2	0.188	1.631	0.012	0.023	1.618	**0.527**

2. Technical Background

To understand the effects of microstructure on the mechanical performance of welds, it is important to recognize microstructural differences at the various weld regions. These include the base metal (BM), heat affected zone (HAZ) and fusion zone (FZ). The FZ is created by heating above the melting point, while the surrounding HAZ material itself consists of several regions which experience thermal cycles with progressively decreasing peak temperature from the fusion boundary. In some of these regions post-weld microstructure depends heavily on the BM structure, while in other regions the BM effects are less clear because peak temperatures during the weld thermal cycle are well above the critical temperature (Ac_3).[10] Thus, it is important to first develop a clear understanding of the thermal history in these regions and their effects on the resulting microstructure.

BM temperatures during welding typically remain below 200°C remote from the weld, so no transformations are activated and the microstructural constituents are left unaffected.[11] Hardness values in the base metal depend mainly on alloying levels and processing methods. All materials used for this study have a ferritic matrix; however, different chemistries and processing result in different strengthening phases among the various AHSS, including: carbides, bainite and martensite.

The HAZ can be divided into four subregions: the subcritical (SC), intercritical (IC), fine grained (FG) and coarse grained (CG) heat affected zones. In the SC HAZ, the peak temperature is below the Ac_1 resulting in tempering of metastable bainite and martensite with an eventual coarsening of carbides. Peak temperatures in the IC HAZ range between Ac_1 and Ac_3.[11,12] Austenitization begins in concentrations of austenite stabilizing elements, typically martensite and bainite in DP and TRIP microstructures. Within this range, increasing peak temperature results in an increase in the fraction of ferrite dissolved into austenite. Rapid post-weld cooling, intensified by continuously cooled electrodes,[12] can result in the transformation of the intercritically austenitized grains back into a dual phase martensite-ferrite structure.

Peak temperatures in the FG and CG HAZ exceed Ac_3, resulting in a fully austenitized local structure.[11] In the FG HAZ the short time above Ac_3 limits grain growth, producing an ultra-fine structure upon cooling. However, temperatures in the CG HAZ are well above Ac_3, and growth of austenite grains is facilitated with the extended time spent at elevated temperatures. Subsequent rapid cooling transforms the austenite into a coarse martensitic microstructure, with transformation to martensite aided by the coarsened austenite grain size.

Temperatures in the FZ surpass the liquidus resulting in molten metal during welding.[11] This is followed by rapid cooling which promotes epitaxial solidification of dendrites with directional growth towards the centerline. After welding, the water cooled electrodes help to remove heat from the weld, inducing high initial cooling rates in the solidified weld metal. It has been reported that RSW cooling rates can be up to the order of 10^5 °C/s,[13] while the electrodes are still in contact with the workpiece. Since the alloying levels in AHSS are relatively high, transformation of austenite at high cooling rates typically results in martensite or bainite.

3. Experimental Methods and Conditions

3.1 Material

The grade and chemical composition of the materials used in this study are shown in Table 1. AHSS include two grades of DP, DP600 and DP780, plus TRIP780 and 590R. HSLA material is also included to represent conventional high strength steels and benchmark AHSS performance. This particular TRIP steel used Si to stabilize the retained austenite. Calculated carbon equivalence for each material, using the equation proposed by Yurioka *et al.*[14] is also included in Table 1.

Prevention of galvanic corrosion for most steels is facilitated with a zinc coating. Table 1 also includes the type and weight of Zn-coatings. Studies have shown during RSW of Zn coated steel annular zinc braze forms at the faying surface around the FZ.[15] Furthermore during the first two cycles of resistance welding the molten coating is pushed away from the FZ.[16]

3.2 Welding equipment and parameters

The spot welded samples were produced using a Center-Line Ltd. 250-kVA pneumatically operated 60 Hz single phase AC RSW machine with constant current control. A truncated class 2 electrode with 6.0 mm face diameter was used as per AWS standards for sheet thickness ranges used in this study.[17] Cooling water flow rate and hold time also followed AWS recommendation of 4 L/min and 5 cycles, respectively. It should be noted that the standard recommended practice of prompt electrode release (5 cycles after termination of weld current) as used here

results in discontinuous cooling curves which can significantly increase the complexity of the steels' metallurgical response.

RSW samples were produced over a range of force, current, and time parameters. A weldability test was conducted to determine weld lobes which produce acceptable weld quality as determined by AWS standards.[17] The weld current was varied from 7 to 10 kA, the weld force ranged from 3.5 to 5.5 kN, and the weld time was between 10 and 20 cycles for each material. The weld parameters were optimized for tensile shear strength and button size as determined by AWS.[17] The weld samples were subjected to overlap tensile shear testing, coach peel testing, and metallographic examination. A total of 11 tests were conducted per condition to facilitate 5 tensile tests, 5 coach peel tests and 1 metallographic cross-section.

3.3 Mechanical testing and microstructure

Welds were fractured using both, tensile shear and coach peel test methods. During coach peel testing, the welded sheets were peeled apart resulting in a force normal to the nugget and inducing failure around the weld. This technique is often used to facilitate nugget diameter measurements. Joint mechanical properties were evaluated by measuring the peak load to failure during overlap tensile shear testing, where the force was applied parallel to the nugget. Care was taken to maintain co-planar alignment during mechanical testing. The fracture surfaces of broken overlapped shear and coach peel tests specimens were examined under a microscope.

Microhardness testing was conducted using a Clemex MT-2001 Vickers microhardness testing machine with a 200 g load and hold time of 15 sec. Microhardness mapping using 0.2 mm grid spacing revealed the hardness distribution and the individual hardness values in selected regions of welded joints.

3.4 Metallographic examination

During metallographic examination all test sections were etched using LePera's reagent to distinguish the different phases.[18] When this particular etchant is used, martensite is etched white, α-ferrite is grey and bainite is black.

3.5 XRD analysis

XRD analysis was facilitated using a Rigaku MSC micro-XRD. The Cu k-alpha x-ray source generated a 1.54 angstrom wavelength. A 0.8 mm collimater was used to irradiate the different welding regions of the TRIP780. Data conditioning and analysis was conducted using the JADE 6.5 software package.

4. Results

4.1 Microstructure and hardness

By examining weld cross-sections, the different regions including BM, HAZ and FZ were revealed. Detailed microstructural observations of these regions are shown for each material in Figs. 1–5. Welding parameters used for each material corresponding to optimal welding conditions are shown in Table 2.

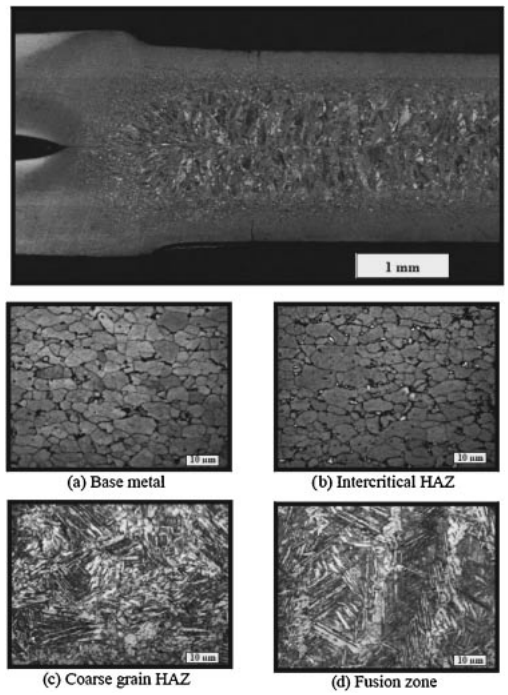

Fig. 1 Microstructure for HSLA.

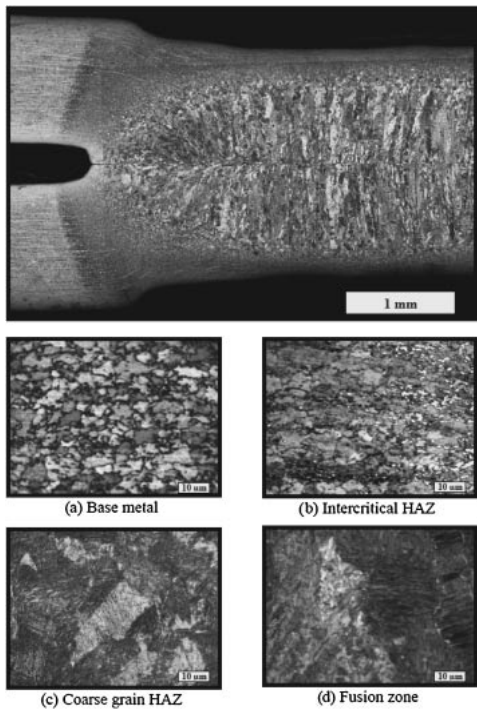

Fig. 2 Microstructure for 590R.

Hardness mapping results for the weld regions including BM, HAZ and FZ are shown in Figure 6 to 10. Each material showed an increased FZ hardness relative to the BM values. All of the examined steels produced FZ hardness values exceeding 350 Hv except for the HSLA which exhibited values near 300 Hv. Detailed analyses of hardness values and microstructural constituents in these regions are given in the following sections.

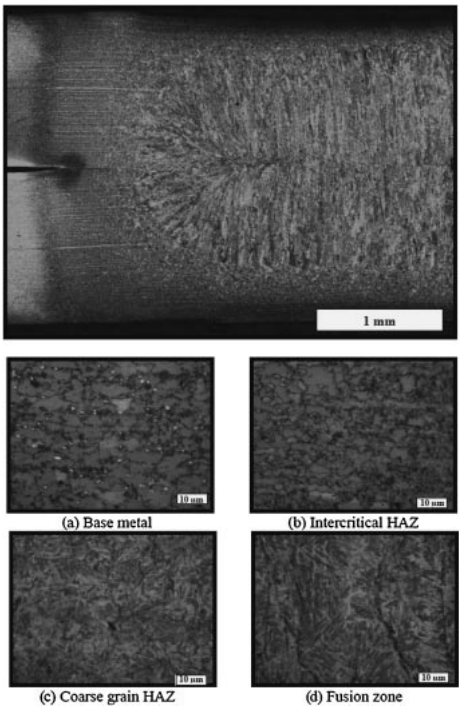

Fig. 3 Microstructure for DP600.

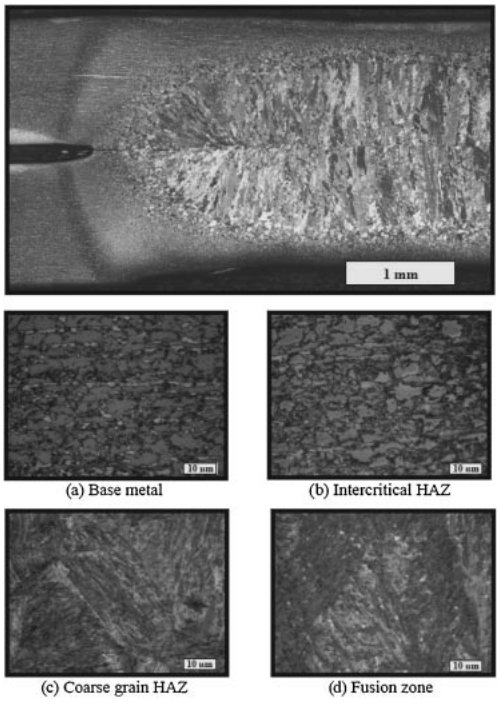

Fig. 4 Microstructure for DP780.

4.1.1 Base metal

The HSLA microstructure, shown in Fig. 1(a), consisted of a ferrite matrix with dispersed carbides at the grain boundaries. The resulting hardness was about 150 Hv. Figure 2(a) shows how the 590R had a similar base structure comprising of a ferrite matrix; however, within the matrix were islands of bainite acting as the strengthening phase. Hardness values for the richer chemistry 590R were slightly higher than HSLA, ranging from 170 to 200 Hv.

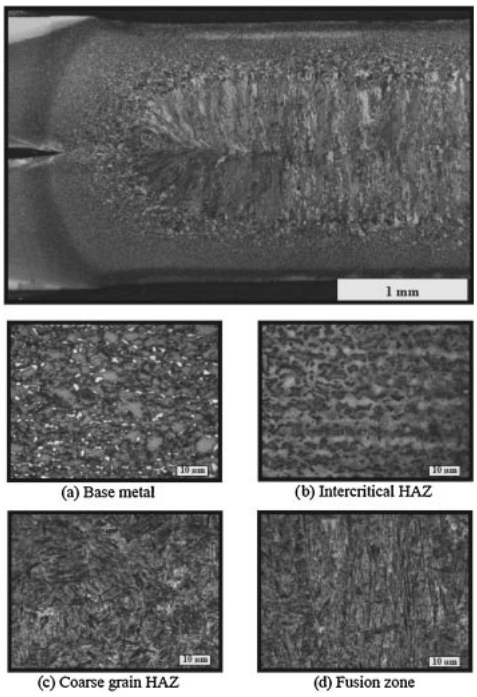

Fig. 5 Microstructure for TRIP780.

Table 2 Optimal Welding Conditions.

	Welding condition		
	Force (kN)	**Current (kA)**	**Time (cycles)**
TRIP 780	4.5	8	20
HSLA	3.5	9	20
DP780	5.5	9	15
DP600	3.5	8	20
590R	5.5	9	20

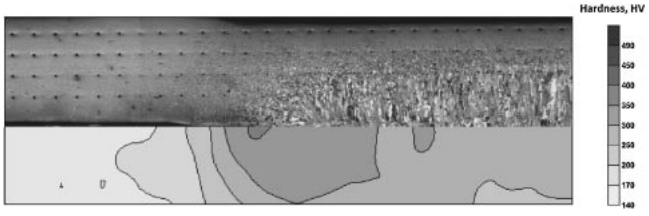

Fig. 6 Hardness mapping of HSLA.

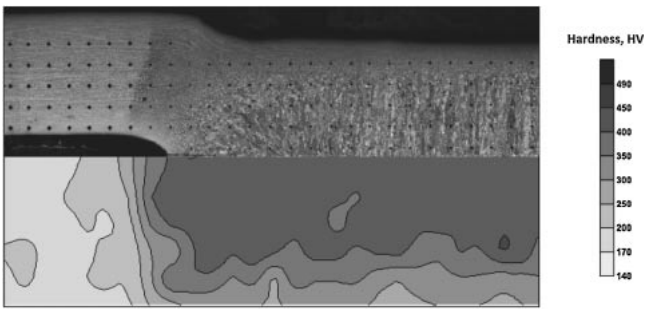

Fig. 7 Hardness Mapping for 590R.

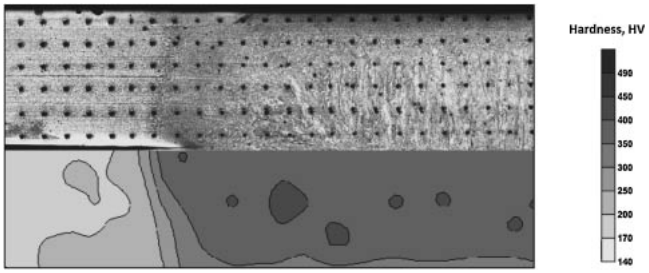

Fig. 8 Hardness Mapping of DP600.

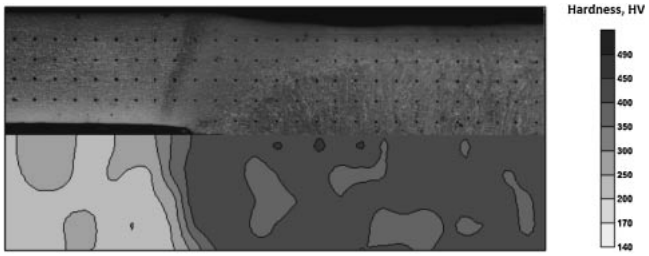

Fig. 9 Hardness Mapping for DP780.

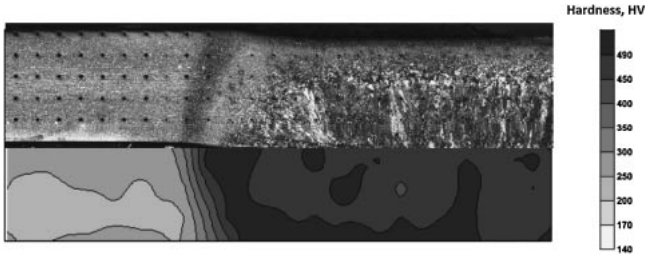

Fig. 10 Hardness Mapping of TRIP780.

The DP600 and DP780 steels, shown in Figs. 3 and 4, respectively, had a ferritic matrix with dispersed martensite at the grain boundaries. The volume fraction of martensite was greater within the DP780 compared to the DP600, resulting in increased strength and greater hardness: 250 Hv to 170 Hv, respectively. The DP780 base metal showed a banded structure of martensite within the base metal. This banding was aligned with the rolling direction; compared to the uniformly dispersed martensite observed in the DP600. The difference in martensite volume fraction and dispersion in the DP base metal was due to varying chemistries and processing used in manufacturing.[19)]

The TRIP780 BM consisted of a relatively complex microstructure, see Fig. 5(a). It was comprised of a ferrite matrix with retained austenite and finely dispersed bainite. Hardness distributions revealed that the centreline was slightly softer than the top and bottom surfaces. The outer edge hardness was above 200 Hv while the center values were slightly lower, which can be attributed to production methods used during processing.[20)] The TRIP780 had the highest BM hardness values of all the steels tested in this study.

4.1.2 Intercritical heat affected zone

In the HSLA IC HAZ, shown in Fig. 1(b), carbides situated at the ferrite grain boundaries were dissolved in austenite during the weld thermal cycle. The resultant microstructure after cooling consisted of martensite islands (white) formed by decomposition of the C-rich austenite regions. This caused an increase in hardness, which exceeded 170 Hv. The 590R also experienced a similar transformation, with the austenitized bainite transforming into martensite islands, increasing the hardness to above 200 Hv, as shown in Fig. 7.

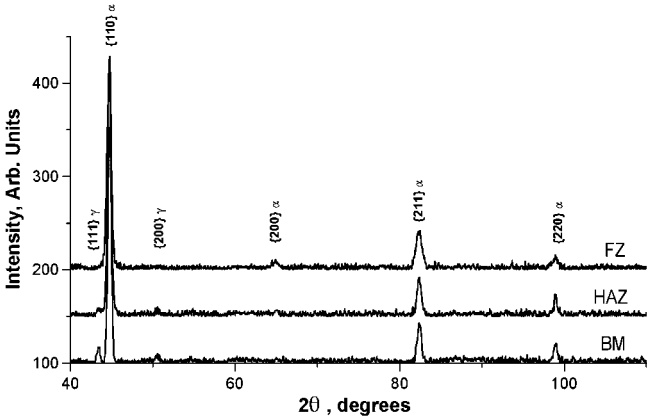

Fig. 11 XRD results for BM, HAZ and FZ of TRIP spot weld.

In the IC HAZ of DP alloys there was a coarsening of the martensite phase. Where peak temperatures just exceeded Ac_1, dissolution of martensite was initiated, which was then rapidly cooled. Moving towards the FZ, the peak temperature increased, increasing the fraction of ferrite that was dissolved into austenite. This increased the volume fraction of martensite, with hardness values rising above 200 Hv and 250 Hv for DP600 and DP780, respectively. As peak temperatures approached Ac_3, almost all of the ferrite was dissolved into austenite. Post-weld rapid cooling subsequently formed a nearly fully martensitic structure.

Figure 5(b) shows that the microstructure in the TRIP780 IC HAZ contained ferrite and a white banded structure. Variations of shading within the banded structure suggest an inhomogeneous composition resulting in differing intensities of chemical attack by etchants. To clarify the metallographic results, the TRIP samples were analyzed using XRD to clarify the phases present in all of the weld zones. The XRD revealed traces for BM, HAZ and FZ of TRIP780 are shown in Fig. 11. BM analysis showed peaks for austenite and ferrite, which are the main constituents observed using metallographic examinations. Within the HAZ a reduction in intensity for the austenite peaks and a slight increase in BCT martensite was observed. This transition can pertain to a combination of austenite and martensite in the HAZ, suggesting the coexistence of both phases within this region. XRD readings of the FZ produced no evidence of austenite peaks, hence the structure was predominately martensitic as observed by optical microscopy.

4.1.3 Coarse grain HAZ

The microstructures of the CG HAZ regions are shown in Figs. 1(c)–5(c). The HSLA showed a needle like structure consisting of sideplate ferrite with strips of grain boundary ferrite. In all of the examined AHSS, the CG HAZ microstructure was mainly comprised of blocky martensitic grains with hardness similar to the FZ. The peak hardness values for

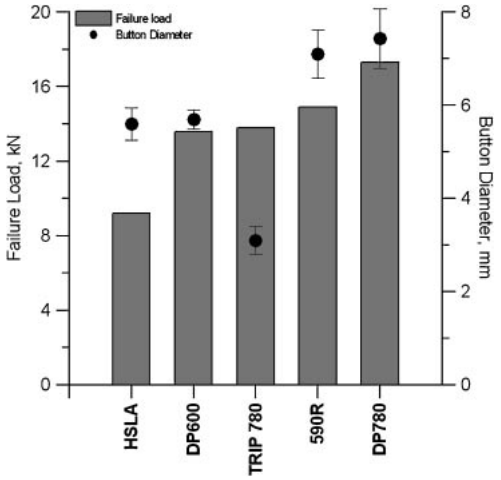

Fig. 12 Mechanical Properties of Weldment.

the TRIP780 within the CG HAZ surpassed 490 Hv. Excess hardness in the CG HAZ can be concerning if fracture toughness is reduced.

4.1.4 Fusion zone

The FZ microstructures, shown in Figs. 1(d)–5(d), were characterized by the columnar nature of solidification and needle-like martensite; however, the hardness values varied for each material. HSLA FZ hardness values were the lowest out of all the materials tested, ranging 250–350 Hv as shown in Fig. 6. 590R and DP600 exhibited similar strength and BM hardness values; however FZ hardness values were considerably different, 400–450 Hv and 350–400 Hv, respectively. For the DP780 FZ hardness was similar to the 590R, ranging between 400–450 Hv. Maximum hardness values were attained from the TRIP780 which exhibited values above 450 Hv. Martensite hardness is expected to range above 350 Hv for carbon contents in excess of 0.05 mass %.[21] Hence, FZ hardness values for the AHSS are well within the expected martensite hardness range.

4.2 Mechanical properties

Welds were made using the parameters shown in Table 2. These conditions produced weldments exhibiting the highest tensile shear properties within the lobe domain. Mechanical properties of the welds are given in Fig. 12. The highest and lowest tensile properties were exhibited by DP780 and HSLA, respectively. Comparable failure loads were achieved for DP600, 590R and TRIP780. Trends mainly reflect those observed with button diameters; failure loads increased with button diameter. However, the TRIP780 produced a notably reduced optimal button size compared to the other AHSS. It is also noted that the HSLA required the highest current and time at a relatively low force to attain the optimal weld. This is likely due to the lower resistivity of HLSA, which demands increased time and current compared to AHSS.

Fracture surfaces for coach peel and tensile testing of each material are shown in Fig. 13 and Fig. 14, respectively. Peel testing resulted in full button fracture for all material except TRIP780 which exhibited a partial interfacial fracture mode. During tensile shear testing DP600 produced interfacial failure modes; while HSLA, 590R, DP780 and TRIP780 resulted in pull-out fracture modes.

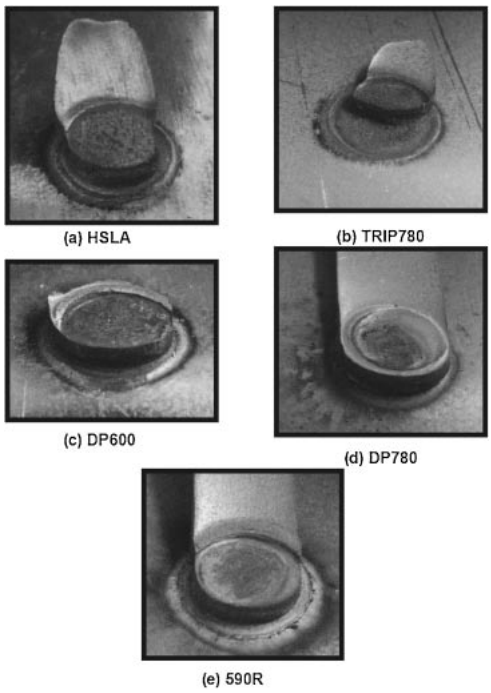

Fig. 13 Fracture surface for coach peel test specimens.

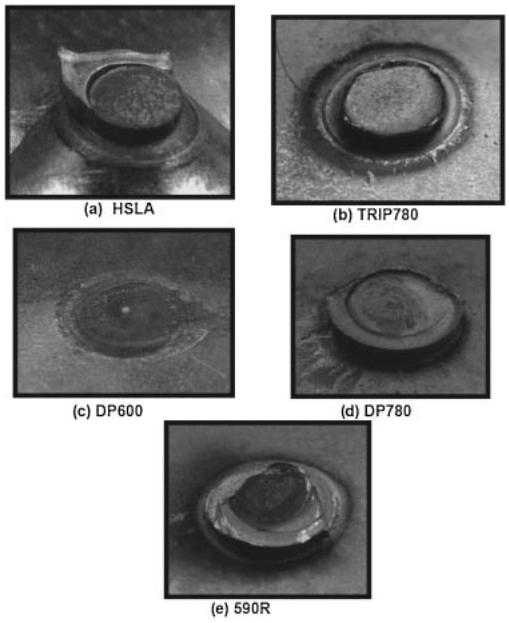

Fig. 14 Fracture surface for overlap tensile shear specimens.

5. Discussion

5.1 Fracture surfaces

Coach peel testing resulted in full button failure for all tested materials with exception of TRIP780, which produced a partial interfacial fracture. Closer examination shows a crescent-shaped interface (Fig. 13(b)) with remnants of the joined sheet. Previous studies have shown inhomogeneity of alloying elements within the fusion zone,[22] mainly evident for rich chemistry steels such as TRIP. Segregation of alloying elements during solidification can provide a path for

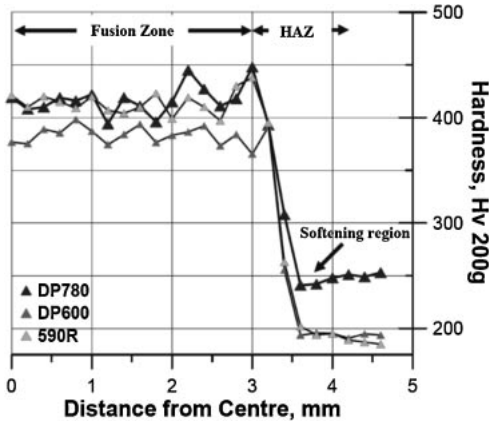

Fig. 15 Hardness trace from BM to FZ.

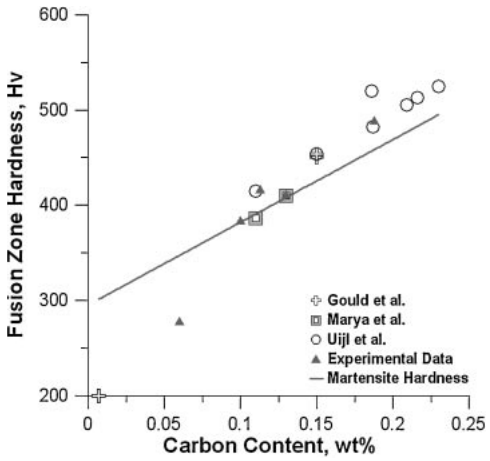

Fig. 16 Carbon content Vs Vickers Hardness.

fracture propagation that follows along dendrite boundaries. Partial tensile fracture can occur, leading to significantly reduced button diameters during coach peel testing due to the application of a force normal to the nugget.

Fracture surfaces for tensile shear test results revealed a combination of interfacial and button pull-out failure modes as shown in Fig. 14. Button pullout failure modes occurred for HSLA, 590R, DP780 and TRIP780. DP600 produced interfacial failure, indicating fracture initiation at the interface and propagation through the centerline. Khan *et al.*[23] showed the relationship between bonded area and failure loads with occurrence of interfacial fracture. However during button pull-out, material properties and FZ diameter are the main determining factors of spot weld strength. Furthermore, failure paths for tensile shear testing of each of these steel has been detailed in a separate publication.[9]

Significant differences in failure modes were observed for the two DP alloys tested. The DP600 underwent interfacial fracture while the DP780 produced a full button. Xia *et al.*[24] showed the effects of HAZ softening occurring for various DP alloys due to post-weld tempering. Higher grades of DP exhibit greater potential for HAZ softening due to larger volume fraction of martensite which experiences post-weld tempering. In the current study failure was found to occur near the HAZ for the higher grade DP780 compared to interfacial failure occurring for the DP600. BM microstructures for the dual phase alloys in Fig. 3(a) and Fig. 4(a) showed a higher volume fraction of martensite in the DP780 making it more susceptible to HAZ softening. A detailed hardness trace from the BM to the FZ for the DP alloys is shown in Fig. 15. The DP780 exhibited HAZ softening compared to the DP600. Tempering of martensite within the DP780 base metal structure therefore evidently promoted HAZ failure while the lack of softening in DP600 may have contributed to interfacial failure.

5.2 Fusion zone hardness

The characteristic features of columnar grains growing towards the centerline and a largely martensitic microstructure are common to all the steel types shown in Figs. 1(d)–5(d). Results have shown the FZ for rich chemistry steels (DP and TRIP) to consist mainly of martensite. Leaner chemistry HSLA showed a mixed FZ microstructure (martensite and bainite), which is likely due to differences in the HSLA CCT diagram compared to the AHSS. CCT diagrams for leaner HSLA are usually shifted towards the left. In these experiments, the early electrode release and resulting decrease in cooling rate could bring the bainite nose within the transformation time to start bainite nucleation in the FZ during RSW. However, all of the AHSS showed a fully martensitic FZ microstructure and so as expected the FZ hardness is mainly a function of alloy levels within the steel.

Carbon, as an austenite stabilizer, increases the ability to form martensite (hardenability), and is also known to increase the hardness of martensite. Using carbon content to predict martensite hardness was viable for traditional lean chemistry steels, which mainly contained only iron and carbon and low levels of other alloying elements. Yurioka *et al.* measured martensite hardness of various basic oxygen converter (BOC) steels produced using high cooling rates achieved from arc welding.[25] Using this experimental data the following relationship was derived:

$$H_M = 884C(1 - 0.03C^2) + 294 \quad (1)$$

Where H_M is martensite hardness and C is carbon content.

Figure 16 shows the FZ hardness as a function of carbon content for data from this work as well as data from other researchers. Calculated fusion zone martensite hardness attained from Equation 1 is also plotted. There were 5 steels studied in this work with a carbon range from 0.06 to 0.188 mass%. This figure is further populated using experimental data from several sources including Marya *et al.*,[7] Gould *et al.*[26] and Uijl *et al.*[22] who have also done work in this area.

Examination of Fig. 16 shows an over-prediction of hardness values for lower carbon steels, which includes an interstitial free (IF) steel alloy and the tested HSLA. Deviation from predicted values can be attributed to a mixed martensite-bainite microstructure in the FZ of these steels. Since Equation (1) was developed for martensitic structures, an over-prediction can occur when applied to lower carbon steels which do not form a fully martensitic structure. However the intermediate chemistry steels show a relatively good agreement to eq. (1).

Higher carbon steels, including AHSS, show higher FZ hardness than the predicted values. These steels also contain higher concentrations of alloying elements such as Mn, Mo, Si and Al. The effects of these elements on the RSW FZ hardness are not yet fully understood and further research is required to detail their influence. However, it known that the addition of some alloying elements can enhance the effectiveness of carbon in martensite.[27,28] Also, other studies have suggested secondary hardening, due to the formation of carbides during tempering, resulting in increased material hardness.[29] Since the early electrode release used here evidently caused a significant reduction in final cooling rate for these welds, the martensite formed in the FZ and CG HAZ was likely auto-tempered to some degree, thus enhancing the influence of alloying additions other than carbon on the final hardness.

The carbon equivalence (CE) value of transformable steels is an index measure which predicts a materials susceptibility to post-weld cold cracking in the HAZ. The susceptibility to cold cracking is directly related to the amount and hardness of martensite within the HAZ. Alloying elements can aid in the formation of martensite by retarding the kinetics of ferrite and bainite formation, and hence the CE provides an index measure of the effects that alloying elements have on steel hardenability.

Multiple CE equations are available in literature[30–32] each taking into account numerous alloying elements, which include both ferrite and austenite stabilizers. Available equations include the CE_{IIW}[30] and P_{cm} developed by Ito *et al.*[31] Studies have shown the CE_{IIW} to better suit higher carbon steels with greater then 0.16% carbon.[33] P_{cm} on the other hand is more appropriate for low-carbon low-alloy steel.[14] However the wide range of carbon contents found in AHSS can not be accommodated using one simple equation.

Yurioka *et al.*[34] used various test methods to determine preheating temperatures required to avoid cold cracking during welding. In particular, the stout slot weld tests were carried out on 20 different steels.[35] The steels had various structural applications with each containing various amount of alloying elements. From this work the following equation was proposed:

$$CE_Y = C + A(C)\cdot\left\{5B + \frac{Si}{24} + \frac{Mn}{6} + \frac{Cu}{15} + \frac{Ni}{20} + \frac{Cr + Mo + Nb + V}{5}\right\} \quad (2)$$

where

$$A(C) = 0.75 - 0.25\tan h\{20(C - 0.12)\}$$

CE_Y is the Yurioka carbon equivalence and $A(C)$ is an accommodation factor. Equation (2) contains an accommodation factor, which approaches 0.5 when carbon is below 0.08% and increases to 1.0 with carbon contents above 0.18%. The accommodation factor eliminates the use of two CE equations and allows for CE_Y to be applicable for steels alloys with carbon contents ranging between 0.02 and 0.2. Furthermore this single equation can accommodate the unique chemistries of most AHSS.

Alloying elements can aid the formation of martensite by increasing minimum cooling times, hence the CE provides an effective means of measuring the how alloying affects martensite formation. Figure 17 shows the relationship between FZ hardness and carbon equivalence calculated using CE_{IIW} and P_{cm} for the appropriate carbon range. Considerable scatter is observed for the CE_{IIW} and P_{cm} equation. Using a linear regression fit, an attempt was made to find a correlation between carbon equivalence and FZ hardness. However there is minimal agreement and the scatter is reflected in the relatively low linear correlation coefficient value ($r = 59.36\%$).

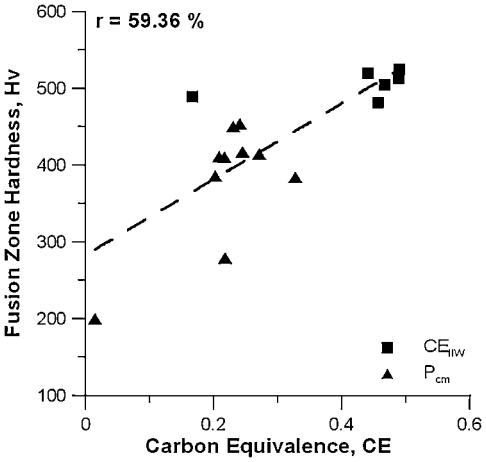

Fig. 17 Fusion zone hardness Vs P_{cm} and CE_{IIW}.

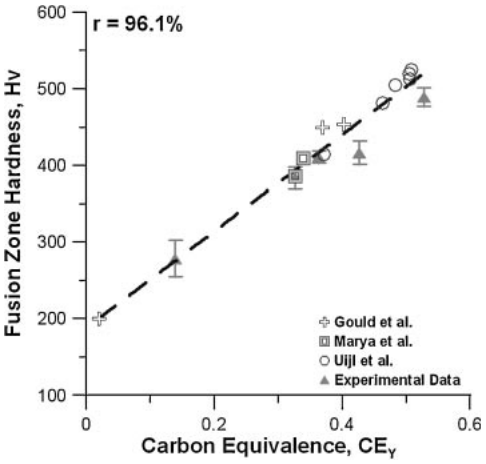

Fig. 18 CE_Y Vs Fusion Zone Hardness.

CE_Y and average FZ hardness are plotted in Fig. 18 for each steel alloy. Trends show FZ hardness increases with richer chemistries that produce higher CE values. CE_Y shows an improved linear relationship between fusion zone hardness and base material chemistry ($r = 96.1\%$). Extracting the linear relationship between FZ hardness and CE gives the following equation:

$$Hv_{FZ} = 630CE_Y + 188 \quad (3)$$

Where Hv_{FZ} is fusion zone hardness and CE_Y is carbon equivalence calculated using eq. (2).

Equation (3) provides an improved method for determining the RSW FZ hardness of steels. Compared to eq. (1), Equation 3 accounts for various alloying elements used in

the production of AHSS. By using the Yurioka *CE* equation, which includes an accommodation factor for a wide range of chemistries, a more reliable relationship between RSW FZ hardness and chemistries can be made, for the particular resistance welding conditions used here.

6. Conclusions

The current study examined the microstructure and mechanical properties of RSW AHSS. Using standard optimization methods, weldments were made using the optimal weld conditions and compared as to resultant structure and properties. The AHSS consistently achieved high tensile strength compared to the conventional HSS. Microstructural observations were presented for the different weld regions of each material. Furthermore, the microstructural observations and hardness testing revealed predominately harder microstructures within the FZ of the AHSS, which increased with richer chemistry steels. Finally, an equation to approximate FZ hardness in RSW was proposed. Some key conclusions include:

(1) The typical IC HAZ microstructure comprised of undissolved ferrite and dispersed martensite islands. The TRIP steel exhibited some retained austenite within the IC HAZ.

(2) The FZ and CG HAZ were mainly comprised of martensite for the rich chemistry AHSS alloys. The leaner chemistry HSLA showed areas of ferrite and bainite in the CG HAZ, while bainite and martensite was observed in the FZ.

(3) Materials having elevated carbon equivalence experience increased FZ hardness indicating a strong correlation between chemistry and mechanical properties.

(4) The sole use of carbon content was shown to be insufficient in predicting FZ hardness of these resistance welds. The Yurioka *CE* equation was found to be well correlated with FZ hardness values and BM chemistries. FZ hardness can be estimated for a single pulse weld with a 5 cycle hold time using the following equation:

$$Hv_{FZ} = 630^{*}CE_{Y} + 188$$

(5) AHSS produced superior tensile failure loads relative to HSLA. Interfacial fracture was observed during tensile testing of DP600; while button pullout failure modes occurred for HSLA, 590R, DP780 and TRIP780.

REFERENCES

1) K. Banerjee and U. K. Chatterjee: Metall. Mater. Trans. A **34A** (2003) 1297–309.
2) S. Dinda, C. Belleau and D. K. Kelley: International Conference on Technology and Applications of HSLA Steels (ASM, 1984) pp. 475–483.
3) J. Dufourny and A. Bragard: Welding in the World **23**, No. 5–6, (1985) 100–123.
4) Y. Omiya *et al.*: R & D Kobe Steel Engineering Reports, **52**, No. 3 (2002) 10–14.
5) T. B. Hilditch, D. K. Matlock, B. S. Levy and J. F. Siekirk: S.A.E. transactions [0096-736X] **113** (2005) Iss:Section 5.
6) R. G. Davies: Metall. Mater. Trans. A **9A** (1978) 671–679.
7) M. Marya and X. Q. Gayden: Welding Journal **85**, No. 11 (2005) 172s–182s.
8) W. Tong, H. Tao, X. Jiang, N. Zhang, M. P. Marya, L. G. Hector and X. Gayden: Metall. Mater. Trans. A **36** (2006) 2651–2669.
9) M. I. Khan, M. L. Kuntz and Y. Zhou: Science and Technology of Welding and Joining **13** (2008) 49–59.
10) S. J. Hu, J. Senkara and H. Zhang: Proc. of International Body Engineering Conf. IBEC'96, Body and Engineering Section, Detroit (MI), (1996), p. 91.
11) S. Kou: *Welding Metallurgy*, 2nd Ed., (J. Wiley & Sons, Inc., Hoboken, NJ, 2003).
12) H. Zhang and J. Senkara: *Resistance Welding: Fundamentals and Applications*, (CRC Group, Boca Raton, FL, 2006)
13) C. M. Adams: Welding Journal **37**, No. 5, (1958) 210s–215s.
14) H. Suzuki: Trans. Japan Welding Society **10** (1979) 82–91.
15) S. A. Gedeon and T. W. Eagar: Metall. Mater. Trans. B **17B** (1986) 887–901.
16) W. Tan, Y. Zhou and H. W. Kerr: Metall. Mater. Trans. A **33A** (2002) 2667–2676.
17) ANSI/AWS/SAE/D8.9-97: *Recommended Practices for test methods for evaluating the resistance spot welding behavior of automotive steels*, (1997).
18) F. S. Lepera: Journal of Metals **32**, No. 3, (1980) 38–39.
19) F. G. Caballero, G. Andrea, C. Carlos and D. C. Garcia: Mater. Trans. **47** (2006) 2269–2276.
20) A. Pichler, S. Traint, G. Amoldner, P. Stiaszny, M. Blaimschein and E. A. Werner: Proc. 44th MWSP Conference Proceedings **35** (2002).
21) W. D. Callister: *Fundamentals of Materials Science and Engineering*, (John Wiley and Sons Ltd, 2004).
22) N. Uijl and S. Smith: Advances in Resistance Welding, Austria (2006) 30–62.
23) M. I. Khan, M. L. Kuntz, P. Su, A. Gerlich, T. North and Y. Zhou: Science and Technology of Welding and Joining **12** (2007) 175–182.
24) M. Xia, N. Sreenivasan, S. Lawson, Y. Zhou and Z. Tian: Journal of Engineering Materials and Technology **129** (2007) 446–452.
25) N. Yurioka, M. Okumura, T. Kasuya and Cotton: Met. Constr. **19** (1987) 217R–223R.
26) J. E. Gould, S. P. Khurana and T. Li: Welding Journal **85**, No. 5 (2006) 111–116.
27) M. D. Perkas: Met. Sci. Heat Treat. **6** (1968) 415–425.
28) H. Cerjak: *Mathematical modelling of weld phenomena 3*, (Maney Publishing, 1997).
29) H. Kwon, C. M. Kim, K. B. Lee, H. R. Yang and J. H. Lee: Metall. Mater. Trans. A **28** (1997) 621–627.
30) British Standard Institute. Dec. 1974 Specification for metal-arc welding of carbon and carbon manganese steels. BS5135.
31) Y. Ito and K. Bessyo: J. of Japan Welding Society **37** (1968) 683–991.
32) J. Dearden and H. O'Niel: Trans. Int. Weld. **3** (1940) 203–214.
33) T. Yatake, N. Yurioka, R. Kataoka and E. Tsunetomi: J. Japan Welding Society **49** (1980) 484–489.
34) N. Yurioka, H. Suzuki, S. Ohshita and S. Saito: Welding Journal **62**, No. 6 (1983) 147–153.
35) R. D. Stout and R. Vasudevan: J. Japan Welding Society **37** (1968) 683–991.